

Oxygen enrichment in carbon-rich planetary nebulae

Gloria Delgado-Inglada^{1*}, Mónica Rodríguez², Manuel Peimbert¹, Grażyna Stasińska³ and Christophe Morisset¹

¹*Instituto de Astronomía, Universidad Nacional Autónoma de México, Apdo. Postal 70264, 04510, México D. F., Mexico*

²*Instituto Nacional de Astrofísica, Óptica y Electrónica (INAOE), Apdo. Postal 51 y 216, 72000 Puebla, Pue. Mexico*

³*LUTH, Observatoire de Paris, CNRS, Université Paris Diderot; Place Jules Janssen, F-92190 Meudon, France*

ABSTRACT

We study the relation between the chemical composition and the type of dust present in a group of 20 Galactic planetary nebulae (PNe) that have high quality optical and infrared spectra. The optical spectra are used, together with the best available ionization correction factors, to calculate the abundances of Ar, C, Cl, He, N, Ne, and O relative to H. The infrared spectra are used to classify the PNe in two groups depending on whether the observed dust features are representative of oxygen-rich or carbon-rich environments. The sample contains one object from the halo, eight from the bulge, and eleven from the local disc. We compare their chemical abundances with nucleosynthesis model predictions and with the ones obtained in seven Galactic H II regions of the solar neighbourhood.

We find evidence of O enrichment (by ~ 0.3 dex) in all but one of the PNe with carbon-rich dust (CRD). Our analysis shows that Ar, and especially Cl, are the best metallicity indicators of the progenitors of PNe. There is a tight correlation between the abundances of Ar and Cl in all the objects, in agreement with a lockstep evolution of both elements. The range of metallicities implied by the Cl abundances covers one order of magnitude and we find significant differences in the initial masses and metallicities of the PNe with CRD and oxygen-rich dust (ORD). The PNe with CRD tend to have intermediate masses and low metallicities, whereas most of the PNe with ORD show higher enrichments in N and He, suggesting that they had high-mass progenitors.

Key words: ISM: abundances – planetary nebulae: general – H II regions – stars: abundances – nuclear reactions, nucleosynthesis, abundances.

1 INTRODUCTION

Planetary nebulae (PNe) are the final products of many stars with masses below $\sim 8 M_{\odot}$. This evolutionary stage occurs after the asymptotic giant branch (AGB) phase, if the star reaches a temperature high enough to ionize the circumstellar gas (the AGB external envelope ejected through a stellar wind) before it dilutes into the interstellar medium. The ionized gas contains valuable information on the nucleosynthesis processes occurring inside the AGB stars (because some elements are produced in the interior of these stars and then carried to the surface) and on the chemical composition of the environment where the star was born (since other elements remain unchanged during the life of the star). The chemical abundances in PNe can be compared with the ones computed using the same techniques in H II regions in order to obtain information not only about the efficiency of stellar nucleosynthesis and dredge-up processes but also about the development of chemical evolution in different galaxies.

The oxygen abundance has been traditionally used as a proxy

for the metallicity in ionized nebulae because oxygen is the element for which more reliable abundances can be obtained. Bright emission lines from two of its ionization states, O^+ and O^{++} , can be easily measured in optical spectra, and the correction for the contribution of higher ionization states is large only for PNe of very high excitation. However, AGB stars can modify the oxygen abundance via two mechanisms. The third dredge-up (TDU) is a mixing event that transports to the stellar surface material created by He burning and the *s*-process. The material is heavily enriched in carbon but also has some oxygen (see e.g. Karakas & Lattanzio 2014). On the other hand, hot bottom burning (HBB) occurs in the most massive progenitors and consists in the penetration of the bottom of the convective envelope into a region where the temperature is sufficient to activate the CNO-cycle, which can destroy oxygen (see e.g. Karakas & Lattanzio 2014). The products are then conveyed to the surface.

The efficiencies of the TDU and HBB depend on the initial mass of the star and on its metallicity, and the predictions differ from model to model. For example, standard nucleosynthesis models with no extra mixing processes, such as those of Karakas (2010), do not predict a significant production of oxygen at solar

* E-mail: gloria.delgado.inglada@gmail.com (GDI)

or half solar metallicity. However, models that include diffusive convective overshooting, like those computed by Marigo (2001) and Pignatari et al. (2013), predict a significant production of oxygen, even at solar metallicities. This mixing mechanism was first introduced by Herwig et al. (1997) and causes the convective envelope to penetrate more deeply into the star and, in combination with an efficient third dredge up, leads to an increase of the oxygen abundance for stars between $1.5 M_{\odot}$ and $3 M_{\odot}$. There are other mechanisms that can produce extra mixing, such as rotation, magnetic fields, and thermohaline mixing (see e.g. Karakas & Lattanzio 2014). These mechanisms are not well understood, but reliable determinations of the chemical composition of ionized nebulae might help us to constrain their efficiencies. Observationally, claims of oxygen production in low mass stars have been restricted to low metallicity PNe (see e.g. Péquignot et al. 2000; Leisy & Dennefeld 2006). Rodríguez & Delgado-Inglada (2011) found an overabundance of oxygen in nearby PNe of near-solar metallicity when they compared them with local H II regions, but a detailed analysis of the clues provided by other elements is required in order to ascertain the cause of this overabundance. On the other hand, the AGB models of Karakas (2010) and Pignatari et al. (2013) do not predict a significant destruction of oxygen for metallicities above $Z \approx 0.01$, but the models of Karakas (2010) with $Z \approx 0.008$ show that O/H can decrease by ~ 0.1 – 0.2 dex for stars with masses $M \geq 5 M_{\odot}$, and this effect could also be more important at lower metallicities (see e.g. Stasińska et al. 2010).

Other elements whose abundances we can derive and use as proxies for nebular metallicities are sulfur, neon, chlorine and argon. However, these elements require corrections for the contribution of unobserved ions to their total abundances, the so-called ionization correction factors (ICFs). Up until recently, the available ICFs were based on the similarities of ionization potentials of the ions involved or on the results provided by a small number of photoionization models (e.g. Kingsburgh & Barlow 1994). This problem is now alleviated by the new and more reliable ICFs calculated by Delgado-Inglada, Morisset, & Stasińska (2014), which are based on large grids of models. These new ICFs can be used to derive more reliable estimates of the chemical abundances, including those elements that are expected to be modified during the evolution of the stellar progenitors of PNe, namely, helium, nitrogen, and carbon.

A very useful abundance ratio in the study of PNe is C/O. Its value is related to the initial mass and metallicity of the progenitor star since these parameters determine the efficiencies of the nucleosynthesis processes that change the relative abundances of C and O. Stars are born with $C/O < 1$ ($C/O \approx 0.5$ for solar metallicity; Allende Prieto, Lambert, & Asplund 2002). The lowest mass AGB stars (with initial masses below $\sim 1.5 M_{\odot}$), do not go through the TDU or HBB, and thus keep their C/O values below 1. They are thus defined as O-rich stars. Intermediate mass stars, with masses between ~ 1.5 – $2.0 M_{\odot}$ and ~ 4 – $5 M_{\odot}$ (the mass range depends on metallicity and on the assumptions of the model calculations), suffer the TDU that increases the C abundance in the surface transforming the O-rich star into a C-rich star; these stars have $C/O > 1$. In the most massive progenitors, with masses above ~ 4 – $5 M_{\odot}$, HBB counteracts the effect of the TDU and prevents the formation of a C-rich star; therefore, for these stars one gets again $C/O < 1$.

Moreover, the value of C/O in the atmospheres of AGB stars, which are among the most efficient sources of dust in the Galaxy (Whittet 2010), defines the type of dust grains that are formed. When oxygen is more abundant than carbon, oxygen-rich grains, such as silicates and oxides, will be formed. If carbon is more abun-

dant, other dust species are expected to form, such as SiC, TiC, and MgS. If we assume that the C/O abundance ratio (where C and O are the total abundances of these elements present in dust grains and in the gas) has not changed from the time when dust formation initiated, the type of grains found in PNe will be related to the value of C/O in the atmosphere of the PN progenitor. Therefore, using infrared spectra we can identify different dust grains in PNe and thus classify them as C-rich ($C/O > 1$) or O-rich ($C/O < 1$) PNe. This inference on whether the ejected atmosphere of the progenitor star has C/O above or below 1 can be better than the one obtained with the C/O abundance ratio derived using emission lines, since the latter can be affected by depletion of C or O into dust grains and by the uncertainties involved in its calculation (see e.g. Delgado-Inglada & Rodríguez 2014).

Our aim here is to study the chemical abundances of a group of PNe that have high quality optical and infrared spectra. The optical spectra are used to derive the element abundances and the infrared spectra are used to identify PNe with either oxygen-rich dust (ORD) or carbon-rich dust (CRD). We explore if the two groups of PNe, characterized by different dust grains, show differences in their chemical content. The abundances of the PNe are also compared with the predictions of recent nucleosynthesis models and with the chemical abundances derived for a group of Galactic H II regions.

2 THE SAMPLE

For the purpose of the present study, we need a sample of PNe with high quality spectra (i.e., with a high signal-to-noise ratio and spectral resolution better than 4 \AA), allowing us to perform the usual plasma diagnostics with good precision, to derive accurate abundances of elements that show only weak lines, such as Cl, and to determine (in most cases) the carbon-to-oxygen abundance ratio from very weak recombination lines. Most of the 57 planetary nebulae compiled by Delgado-Inglada & Rodríguez (2014) meet these requirements. From this sample, Delgado-Inglada & Rodríguez (2014) extracted 33 PNe with available infrared spectra. In this paper, we have selected the 20 PNe that we can classify as oxygen-rich or carbon-rich, i.e., objects that have in their infrared spectra either ORD features (amorphous or crystalline silicates) or the broad features around 11 and $30 \mu\text{m}$ associated with SiC and MgS, respectively, that are expected to arise in carbon-rich environments (Whittet 2003). Many of the objects in the sample also show features from polycyclic aromatic hydrocarbons (PAHs), but since PAHs are sometimes detected in PNe with silicates, we do not use these features to classify the PNe as carbon-rich or oxygen-rich. Our selection criterion excludes NGC 2392, that contains dust grains (as can be inferred from the shape of its continuum), but shows no clear evidence of any of the previously mentioned dust features. We also excluded from the analysis PNe like NGC 6884 and NGC 6741 that show PAH emission, but whose available infrared spectra do not allow us to detect or to rule out the presence of silicates or the 11 and $30 \mu\text{m}$ features.

In summary, we use the above information to classify the sample in two groups: 1) ORD PNe are those with silicates and 2) CRD PNe are those with the broad features associated with SiC and MgS. Some of the PNe with ORD and CRD also show emission from PAHs. The so-called dual chemistry PNe are those having PAH emission and silicate dust features (see e.g. Waters et al. 1998). The compilation of dust features is taken from

Table 1. Sample of planetary nebulae

Object	Aliph. C	Arom. C	Silic.	Comments	Ref.
O-rich dust PNe					
Cn 1-5	No	Yes	Yes	[WR]	(1, 7)
DdDm 1	No	No	Yes	...	(2)
H 1-50	No	Yes	Yes	...	(1)
M 1-42	No	Yes	Yes	...	(3)
M 2-27	No	Yes	Yes	wels	(1, 8)
M 2-31	No	Yes	Yes	[WR]	(1, 7)
M 2-42	No	No	Yes	wels	(1, 9)
MyCn 18	No	Yes	Yes	...	(4)
NGC 3132	No	No	Yes	binary	(4, 10)
NGC 6210	No	No	Yes	...	(5)
NGC 6439	No	Yes	Yes	...	(1)
NGC 6543	No	No	Yes	wels	(5, 7)
NGC 7026	No	Yes	Yes	[WR]	(2, 7)
C-rich dust PNe					
Hu 2-1	Yes	Yes	No	...	(2)
IC 418	Yes	Yes	No	...	(6)
M 1-20	Yes	Yes	No	wels	(1, 11)
NGC 40	Yes	Yes	No	[WR]	(5, 7)
NGC 3242	Yes	No	No	...	(4)
NGC 3918	Yes	No	No	...	(4)
NGC 6826	Yes	No	No	binary	(5, 12)

References: (1) Wang & Liu (2007), (2) Wesson, Liu, & Barlow (2005), (3) Liu et al. (2001), (4) Tsamis et al. (2003), (5) Liu et al. (2004a), (6) Sharpee et al. (2003), (7) Tylanda, Acker, & Stenholm (1993), (8) Górný et al. (2004), (9) Depew et al. (2011), (10) Ciardullo et al. (1999), (11) Górný et al. (2009), (12) Méndez (1989).

Comments– [WR]: Wolf Rayet central star, wels: weak emission line star.

Delgado-Inglada & Rodríguez (2014) and is based on *Spitzer* and *ISO* spectra.

The sample of PNe includes objects from the Galactic disc, bulge, and halo. DdDm 1, with a height above the Galactic plane of ~ 7 kpc (Quireza, Rocha-Pinto, & Maciel 2007), is our only object from the halo. Eight PNe belong to the bulge: Cn 1-5, H 1-50, M 1-42, M 2-27, M 2-31, M 2-42, NGC 6439, and M 1-20. These PNe satisfy the three criteria used by Stasińska et al. (1991) to identify bulge PNe, namely, they are located within 10° in terms of latitude and longitude with respect to the Galactic centre, their angular diameters are smaller than $20''$, and their radio fluxes at 6 cm are lower than 100 mJy. The remaining 11 PNe belong to the disc, and a calculation using the distances provided by Zhang (1995) and adopting a solar Galactocentric distance of 8.0 kpc indicates that they have Galactocentric distances between 6 and 9 kpc, so that they can be loosely described as belonging to the solar neighbourhood.

Table 1 lists the 20 PNe studied here with the dust features identified in each of them, some comments about their central stars, and the references from where the optical line fluxes and the characteristics of the central stars have been taken.

In addition to these PNe, we selected from the literature the seven Galactic H II regions from the solar neighbourhood with the best available optical spectra: M8, M16, M17, M20, M42, NGC 3576, and NGC 3603 (Esteban et al. 2004; García-Rojas et al. 2004, 2006, 2007). They cover a range of Galac-

tocentric distances that goes from 6.3 kpc (M16) to 8.65 kpc (NGC 3603), similar to the range covered by the disc PNe.

3 THE ANALYSIS

3.1 Physical conditions

We use the software PyNeb (Luridiana, Morisset, & Shaw 2014) to calculate the physical conditions, the ionic abundances from collisionally excited lines (CELs), and the ionic abundances of He⁺ and He⁺⁺ from recombination lines (RLs). We have selected for our calculations the atomic data listed in Table 2.

We determine two electron temperatures, T_e , for each nebula using the diagnostic ratios [O III] $\lambda\lambda 4363/(\lambda 4959+\lambda 5007)$ and [N II] $\lambda 5755/(\lambda 6548+\lambda 6583)$. We also compute an average density from the available ratios among the following: [O II] $\lambda 3726/\lambda 3729$, [S II] $\lambda 6716/\lambda 6731$, [Cl III] $\lambda 5518/\lambda 5538$, and [Ar IV] $\lambda 4711/\lambda 4740$. For each nebula, the adopted density is the median of the distribution of average values obtained in the Monte Carlo calculations that we use to estimate the uncertainties (see Section 3.4). We prefer to use the median since, in the low and high density limits, it is less affected than the mean by the large changes in the density caused by small variations in the intensity ratios.

When N⁺⁺ is an important ionization state in a nebula, the recombination of this ion may contribute significantly to the intensity of the [N II] $\lambda 5755$ line (Rubin 1986). If this effect is not taken into account, the value of T_e ([N II]) can be overestimated. Liu et al. (2000) derived an expression to calculate this contribution that depends on the N⁺⁺ abundance, and also, to a small degree, on the value of T_e . The N⁺⁺ abundance can be determined using optical RLs, ultraviolet CELs, or infrared CELs, with the choice of lines leading to very different results (see e.g. Liu et al. 2000). Therefore, the size of the correction is somewhat uncertain, and we decided not to use it here. However, we estimate an upper limit to this effect by using the largest possible value for the N⁺⁺ abundance, the one implied by RLs. The most affected objects are the PNe DdDm 1, NGC 3242, and NGC 6826. In the case of DdDm 1, where Wesson et al. (2005) estimate that recombination is the dominant contribution to the emission of [N II] $\lambda 5755$, we could use T_e ([O III]) to derive all the chemical abundances, but we find very similar results. For NGC 3242 and NGC 6826, the corrected values of T_e ([N II]) increase the O/H and Cl/O abundance ratios by ~ 0.2 – 0.6 dex. For the other objects, the corrections are much smaller, leading to changes in our abundance ratios lower than 0.1 dex. These changes, even the larger ones, do not affect in a significant way the conclusions we get from our results below and we will not consider them in what follows.

Table 3 presents the derived temperatures and densities that will be used to compute the ionic abundances.

3.2 Ionic abundances

The ionic abundances of Ar⁺⁺, Cl⁺⁺, N⁺, Ne⁺⁺, O⁺, and O⁺⁺ are computed using the following CELs: [Ar III] $\lambda\lambda 7136, 7751$, [Cl III] $\lambda\lambda 5518, 5538$, [N II] $\lambda\lambda 6548, 6584$, [Ne III] $\lambda\lambda 3869, 3968$, [O II] $\lambda\lambda 3726, 3729$, and [O III] $\lambda\lambda 4959, 5007$, respectively. We do not consider the sulfur ions in our abundance determination because of the still unsolved “sulfur problem”, whereby the values derived in many PNe are found to be systematically lower than those in H II regions of the same metallicity (Henry et al. 2004). We adopt T_e ([N II]) for the calculations involving the single ionized ions and

Table 2. Atomic Data

Ion	Transition Probabilities	Collisional Strengths
O ⁺	Zeppen (1982)	Kisielius et al. (2009)
O ⁺⁺	Storey & Zeppen (2000)	Storey, Sochi, & Badnell (2014)
N ⁺	Galavis, Mendoza, & Zeppen (1997)	Tayal (2011)
S ⁺	Mendoza & Zeppen (1982)	Tayal & Zatsarinny (2010)
S ⁺⁺	Podovedova, Kelleher, & Wiese (2009)	Tayal & Gupta (1999)
Ne ⁺⁺	Galavis et al. (1997)	McLaughlin & Bell (2000)
Ar ⁺⁺	Muñoz Burgos et al. (2009)	Muñoz Burgos et al. (2009)
Ar ⁺³	Mendoza & Zeppen (1982)	Ramsbottom, Bell, & Keenan (1997)
Cl ⁺⁺	Mendoza & Zeppen (1982)	Krueger & Czyzak (1970)

Table 3. Physical conditions

Object	n_e ([O II]) (cm ⁻³)	n_e ([S II]) (cm ⁻³)	n_e ([Cl III]) (cm ⁻³)	n_e ([Ar IV]) (cm ⁻³)	n_e (adopted) (cm ⁻³)	T_e ([N II]) (K)	T_e ([O III]) (K)
O-rich dust PNe							
Cn 1-5	4200 ⁺¹⁷⁰⁰ ₋₁₁₀₀	3000 ⁺²²⁰⁰ ₋₁₅₀₀	2280 ⁺²³⁰⁰ ₋₁₅₀₀	3600 ⁺¹⁴⁰⁰ ₋₁₂₀₀	7400 ⁺¹⁸⁰ ₋₂₀₀	8680 ⁺¹⁶⁰ ₋₁₄₀
DdDm 1	4800 ⁺¹⁶⁰⁰ ₋₁₂₀₀	3900 ⁺⁵¹⁰⁰ ₋₂₄₀₀	4600 ⁺²⁴⁰⁰ ₋₁₅₀₀	12720 ⁺⁴⁷⁰ ₋₆₄₀	12070±320
H 1-50	6700 ⁺²⁵⁰⁰ ₋₁₈₀₀	7500 ⁺³⁷⁰⁰ ₋₂₄₀₀	8900 ⁺⁵⁶⁰⁰ ₋₃₁₀₀	12200 ⁺²³⁰⁰ ₋₁₅₀₀	9300 ⁺²⁵⁰⁰ ₋₁₅₀₀	11280 ⁺⁴⁶⁰ ₋₄₃₀	10870 ⁺²⁴⁰ ₋₂₃₀
M 1-42	1360 ⁺²⁶⁰ ₋₂₀₀	1250 ⁺²⁷⁰ ₋₃₀₀	1520 ⁺⁴¹⁰ ₋₄₀₀	570 ⁺⁵²⁰ ₋₃₁₀	1240±220	8860 ⁺²⁴⁰ ₋₂₁₀	9140±160
M 2-27	7000 ⁺³⁵⁰⁰ ₋₂₁₀₀	12600 ⁺⁹⁶⁰⁰ ₋₄₉₀₀	10700 ⁺¹⁹⁰⁰ ₋₁₄₀₀	10700 ⁺³⁵⁰⁰ ₋₂₄₀₀	9240 ⁺²⁷⁰ ₋₄₅₀	8180 ⁺¹⁵⁰ ₋₁₃₀
M 2-31	6100 ⁺²⁵⁰⁰ ₋₁₅₀₀	6900 ⁺⁴¹⁰⁰ ₋₂₅₀₀	4190 ⁺⁹⁰⁰ ₋₇₁₀	5900 ⁺¹⁷⁰⁰ ₋₁₀₀₀	11380 ⁺⁴⁴⁰ ₋₄₀₀	9760 ⁺¹⁶⁰ ₋₁₈₀
M 2-42	3420 ⁺¹²⁰⁰ ₋₈₅₀	3200 ⁺²⁶⁰⁰ ₋₁₇₀₀	4100 ⁺⁴⁰⁰⁰ ₋₂₈₀₀	3700 ⁺²²⁰⁰ ₋₁₂₀₀	10060 ⁺⁴²⁰ ₋₃₂₀	8410 ⁺¹³⁰ ₋₁₂₀
MyCn 18	5100 ⁺²⁶⁰⁰ ₋₁₃₀₀	9200 ⁺¹⁹⁰⁰ ₋₁₂₀₀	7400 ⁺¹³⁰⁰ ₋₁₁₀₀	10020 ⁺³⁰⁰ ₋₂₉₀	7310 ⁺¹⁰⁰ ₋₁₂₀
NGC 3132	590 ⁺¹⁷⁰ ₋₁₈₀	740 ⁺³⁵⁰ ₋₂₈₀	540 ⁺⁴²⁰ ₋₃₆₀	621 ⁺²⁰⁰ ₋₆₃	9350 ⁺²⁸⁰ ₋₂₂₀	9450 ⁺²⁰⁰ ₋₁₈₀
NGC 6210	4070 ⁺¹⁴⁰⁰ ₋₉₅₀	3240 ⁺¹²⁰⁰ ₋₉₄₀	3810 ⁺⁸⁷⁰ ₋₈₆₀	11750 ⁺³⁹⁰ ₋₄₀₀	9970±290
NGC 6439	3740 ⁺¹¹⁰⁰ ₋₇₃₀	4700 ⁺¹⁹⁰⁰ ₋₁₁₀₀	5060 ⁺⁸⁴⁰ ₋₉₀₀	6070 ⁺¹³⁰⁰ ₋₉₉₀	4980 ⁺⁶⁷⁰ ₋₄₈₀	9630 ⁺³⁰⁰ ₋₂₄₀	10260 ⁺²⁶⁰ ₋₁₆₀
NGC 6543	4500 ⁺¹⁸⁰⁰ ₋₁₀₀₀	5900 ⁺⁵²⁰⁰ ₋₂₁₀₀	4400 ⁺³³⁰⁰ ₋₁₉₀₀	3400 ⁺³²⁰⁰ ₋₂₃₀₀	5100 ⁺²¹⁰⁰ ₋₁₃₀₀	9930 ⁺⁴⁹⁰ ₋₄₉₀	7780 ⁺²²⁰ ₋₂₀₀
NGC 7026	2910 ⁺³² ₋₃₅	26500 ⁺¹³⁰⁰⁰ ₋₈₈₀₀	8800 ⁺¹⁵⁰⁰ ₋₁₃₀₀	5210 ⁺¹¹⁰⁰ ₋₇₁₀	6020 ⁺⁴⁵⁰⁰ ₋₇₈₀	9730 ⁺³⁰⁰ ₋₄₅₀	9130 ⁺¹³⁰ ₋₁₅₀
C-rich dust PNe							
Hu 2-1	9000 ⁺⁶³⁰⁰ ₋₂₆₀₀	28000 ⁺¹⁵⁰⁰⁰ ₋₁₁₀₀₀	11700 ⁺⁹⁴⁰⁰ ₋₄₄₀₀	11790 ⁺⁷⁴⁰ ₋₉₇₀	9600 ⁺²⁰⁰ ₋₂₃₀
IC 418	9000 ⁺⁴⁸⁰⁰ ₋₂₃₀₀	15300 ⁺¹⁶⁰⁰⁰ ₋₆₆₀₀	10400 ⁺¹⁷⁰⁰ ₋₁₈₀₀	4860 ⁺⁸²⁰ ₋₈₅₀	9800 ⁺⁴³⁰⁰ ₋₂₀₀₀	9530 ⁺³⁹⁰ ₋₃₇₀	8780 ⁺¹⁵⁰ ₋₁₉₀
M 1-20	9400 ⁺⁷¹⁰⁰ ₋₂₇₀₀	9300 ⁺⁵⁴⁰⁰ ₋₃₂₀₀	8700 ⁺¹²⁰⁰⁰ ₋₄₇₀₀	10600 ⁺⁶²⁰⁰ ₋₅₈₀₀	10900 ⁺⁴¹⁰⁰ ₋₂₉₀₀	11110 ⁺⁵¹⁰ ₋₆₁₀	9760 ⁺²⁰⁰ ₋₁₉₀
NGC 40	1200 ⁺³⁰⁰ ₋₂₂₀	1840 ⁺⁴⁴⁰ ₋₄₁₀	890±400	1320 ⁺²⁰⁰ ₋₂₁₀	8460 ⁺¹⁵⁰ ₋₂₂₀	10390±160
NGC 3242	2350 ⁺⁶⁹⁰ ₋₅₂₀	1080±420	2100 ⁺⁷⁶⁰ ₋₆₇₀	1860 ⁺⁴⁰⁰ ₋₃₅₀	12170 ⁺⁴⁷⁰ ₋₄₁₀	11710 ⁺²⁸⁰ ₋₂₃₀
NGC 3918	5000 ⁺¹⁹⁰⁰ ₋₁₃₀₀	5480 ⁺¹¹⁰⁰ ₋₆₇₀	5920 ⁺¹²⁰⁰ ₋₈₃₀	5570 ⁺⁹⁷⁰ ₋₆₃₀	10830 ⁺³⁸⁰ ₋₃₂₀	12540 ⁺²⁹⁰ ₋₃₁₀
NGC 6826	1720 ⁺³⁷⁰ ₋₃₁₀	1980 ⁺⁵⁴⁰ ₋₄₆₀	1310 ⁺⁴⁹⁰ ₋₄₂₀	2140 ⁺⁷¹⁰ ₋₆₆₀	1830 ⁺²⁴⁰ ₋₂₅₀	10400 ⁺⁵³⁰ ₋₄₃₀	9200 ⁺¹⁵⁰ ₋₁₂₀
H II regions							
M8	1420 ⁺⁵⁶⁰ ₋₄₀₀	1610 ⁺²³⁰ ₋₁₈₀	1600 ⁺²¹⁰ ₋₂₆₀	3900 ⁺⁵¹⁰⁰ ₋₂₉₀₀	1830 ⁺¹³⁰⁰ ₋₄₄₀	8290 ⁺¹⁴⁰ ₋₁₅₀	8040 ⁺¹⁰⁰ ₋₈₀
M16	1010 ⁺¹⁸⁰ ₋₁₉₀	1420 ⁺²⁹⁰ ₋₂₇₀	1090 ⁺⁴⁶⁰ ₋₄₉₀	1180 ⁺¹⁹⁰ ₋₂₀₀	8310 ⁺¹⁴⁰ ₋₁₆₀	7580±130
M17	450 ⁺¹¹⁰ ₋₈₀	520 ⁺¹⁶⁰ ₋₁₄₀	330 ⁺²⁴⁰ ₋₂₂₀	2100 ⁺⁴⁶⁰⁰ ₋₁₃₀₀	490 ⁺²¹⁰ ₋₁₁₀	8800 ⁺²⁴⁰ ₋₂₂₀	7960 ⁺¹⁰⁰ ₋₁₃₀
M20	230±50	350±100	390 ⁺³⁰⁰ ₋₂₅₀	310 ⁺¹²⁰ ₋₆₀	8250 ⁺¹⁶⁰ ₋₁₅₀	7760 ⁺⁹⁰ ₋₆₀
M42	4930 ⁺¹⁶⁰⁰ ₋₈₄₀	6100 ⁺⁴⁷⁰⁰ ₋₁₈₀₀	5790 ⁺⁴⁵⁰ ₋₃₉₀	4860 ⁺⁹⁹⁰ ₋₈₇₀	5600 ⁺¹²⁰⁰ ₋₆₈₀	10200 ⁺²⁶⁰ ₋₂₃₀	8290 ⁺¹²⁰ ₋₁₃₀
NGC 3576	1470 ⁺²³⁰ ₋₂₄₀	1330 ⁺³⁹⁰ ₋₃₂₀	2430 ⁺¹²⁰⁰ ₋₆₉₀	3000 ⁺¹⁶⁰⁰ ₋₁₃₀₀	2090 ⁺⁵⁷⁰ ₋₃₆₀	8650 ⁺²¹⁰ ₋₁₆₀	8430±40
NGC 3603	2260 ⁺⁴⁷⁰ ₋₄₈₀	4000 ⁺¹⁶⁰⁰ ₋₁₀₀₀	3800 ⁺¹⁶⁰⁰ ₋₁₂₀₀	1700 ⁺²¹⁰⁰ ₋₁₁₀₀	3160 ⁺⁶⁶⁰ ₋₅₁₀	11120 ⁺⁴⁶⁰ ₋₄₉₀	9010 ⁺¹³⁰ ₋₁₃₀

T_e ([O III]) for the double ionized ions; the adopted value of n_e is used in all cases.

The Ar⁺⁺ abundance of DdDm 1 is calculated using the [Ar III] $\lambda\lambda 7135, 7751$ line intensities of Henry et al. (2008) instead of those measured by Wesson et al. (2005), the reference that we use for all the other line intensities for this object. The reason is that the intensities provided by Wesson et al. (2005) for these lines are too low when compared to measurements by other authors (Barker & Cudworth 1984; Clegg, Peimbert, & Torres-Peimbert 1987; Henry et al. 2008), which is unexpected since the angu-

lar diameter of this object (0.6'') is smaller than the slit widths used for the observations. The intensities given by Wesson et al. (2005) imply $12 + \log(\text{Ar}^{++}/\text{H}^+) = 4.99$, whereas the values listed by Barker & Cudworth (1984); Clegg et al. (1987); Henry et al. (2008) cover the range 5.50–5.69.

We use T_e ([O III]) and the average n_e to compute the abundances of He⁺, He⁺⁺, C⁺⁺, and O⁺⁺ from RLs. We calculate He⁺ as the average of the abundances derived from the He I lines $\lambda\lambda 4471, \lambda\lambda 5876, \text{ and } \lambda\lambda 6678$. The only exception is DdDm 1, where we only use the first two lines because the abundance of He⁺ derived from

$\lambda 6678$ is too low. Since the intensity reported by Wesson et al. (2005) for this line is also too low when compared to the measurements of other authors (Barker & Cudworth 1984; Clegg et al. 1987; Henry et al. 2008), we think that there is some problem with the intensities of Wesson et al. (2005) for several lines in the red part of the spectrum, such as [Ar III] $\lambda\lambda 7135, 7751$, He I $\lambda 6678$, and [S II] $\lambda 6716$. The He⁺⁺ abundances are derived using the He II $\lambda 4686$ line. We use the effective recombination coefficients of Storey & Hummer (1995) for H I and He II and those computed by Porter et al. (2012, 2013) for He I.

The abundances of C⁺⁺ are computed using C II $\lambda 4267$ and the case B effective recombination coefficients of Davey, Storey, & Kisielius (2000). As for the O⁺⁺ abundances, we use the total intensity of multiplet 1 of O II, after correcting for the contribution of undetected lines with the formulae of Peimbert, Peimbert, & Ruiz (2005), and the recombination coefficients of Storey (1994). We exclude from our calculations O II lines of multiplet 1 reported as blended in the papers from which we took the line intensities. In the case of NGC 40, there is only one detected O II feature from this multiplet and it is blended with a N III line, thus we prefer to use the abundance of O⁺⁺ derived by Liu et al. (2004b) from other multiplets. For the rest of the PNe, we do not consider other multiplets because their lines are weaker and likely suffer from blends. Indeed, we find that the O⁺⁺ abundances computed only from multiplet 1 are generally lower than those obtained using other multiplets.

The final ionic abundances derived from CELs and RLs and their associated uncertainties (see Section 3.4) are presented in Table 4.

3.3 Total abundances

To obtain total elemental abundances one needs to take into account the contribution of unobserved ions by using ICFs. Many studies still use ICFs based on similarities of ionization potentials. Those however ignore the fact that a small difference in the ionization potential may lead to a significant change in the ionization structure (e.g. Simón-Díaz & Stasińska 2008; Delgado-Inglada et al. 2014), and that the ionization structure is not only governed by the spectral energy distribution of the stellar radiation field but also by the importance of recombination and charge exchange reactions. Photoionization models allow a much better estimate of ICFs. For PNe, the ICFs proposed by Kingsburgh & Barlow (1994) have been used for two decades. However, there is no real documentation on how they were obtained and there is no estimate of their uncertainties. A set of formulae has been proposed recently by Delgado-Inglada et al. (2014), based on an extensive grid of *ab initio* photoionization models aiming at representing the whole manifold of PNe. The large set of considered photoionization models allowed, for the first time, an estimation of the error bars on ICFs. They are computed using the analytical expressions provided by Delgado-Inglada et al. (2014), which are based on the maximum dispersion of each ICF obtained from the grid of photoionization models. Those ICFs were tested by applying them to a large sample of PNe and checking that the derived abundance ratios did not depend on the degree of ionization of the objects.

The sample of PNe considered here is a specific sample excluding high density objects and objects ionized by very hot stars. We therefore checked if the ICFs from Delgado-Inglada et al. (2014), which were obtained by considering a wider sample of physical conditions, remain valid for the restricted subsample of photoionization models better representing our observational sam-

ple, i.e., we discard the models with very high gas density or with ionizing stars of very high effective temperatures. We found that the ICFs presented in Delgado-Inglada (2014) remain valid for the restricted subsample of models, both as regards the analytical formulae for the ICFs and as regards the error estimates.

We thus adopted the ICFs derived by Delgado-Inglada et al. (2014) to calculate the abundance ratios Ar/O, C/O, Cl/O, Ne/O, He/H, and O/H. The ICF for O is based on He⁺⁺/(He⁺+He⁺⁺), the ICFs for Ar, C, Cl, and He are based on O⁺⁺/(O⁺+O⁺⁺), and the ICF for Ne is based on both ratios. As for N, we show here the results obtained with the ICF derived by Delgado-Inglada et al. (2014) as well as those derived with the widely used ICF, N/O = N⁺/O⁺ (which are the ones listed in Table 5). We will discuss the differences between both estimates of N/O in section 4.5.

For the H II regions we are considering in this paper, the situation is a priori worse. Formulae for ICFs based on photoionization models have been proposed by Izotov et al. (2006), but they were proposed and tested for giant extragalactic H II regions, and there is a priori no reason why they should apply to slit observations of nearby dense H II regions, some of them ionized by single stars. In fact, we find that they introduce a dependence of the total abundances of argon and neon on the degree of ionization for the H II regions in our sample. In absence of any adequate set of ICFs, we used for our H II regions the same expressions that we used for our PNe. In principle, we could trim the grid of models built for PNe to retain only those that would be adequate for the H II regions we consider (ie. remove the models with effective temperatures above 50000 K and all those that have a shell structure or are density bounded) and use the trimmed grid to compute ICFs that would be relevant for our sample of H II regions. In practise, we checked that the formulae given by Delgado-Inglada et al. (2014) actually fit the trimmed grid quite well (except for the determination of Ar/O in objects where O⁺⁺/(O⁺+O⁺⁺) is larger than 0.5, where the resulting bias on Ar/O can go up to ± 0.09 dex).

One important advantage of the ICFs used here to determine the Cl and Ar abundances is that they can be used when only lines of Cl⁺⁺ and Ar⁺⁺, respectively, are observed. These ions can be analysed using relatively bright lines in the optical spectrum, which makes it easier to achieve a homogeneous calculation of the total abundances. Other ICFs in the literature include more ions that have relatively weak emission lines, such as the [Ar IV] $\lambda\lambda 4711, 4740$ lines in some objects, or that lie in a spectral range that it is not often observed, such as [Cl II] $\lambda 9122$. Moreover, we found, from the grid of photoionization models computed in Delgado-Inglada et al. (2014), that the other ICFs in the literature for Ar and Cl introduce a higher dispersion in the derived abundances.

As for the O/H values computed from RLs, for the H II regions we adopt those provided by Esteban et al. (2005). They are based on the O⁺ and O⁺⁺ abundances derived with O I and O II RLs for some objects; for other objects O I RLs could not be measured properly and the O⁺ abundances are based on the abundances implied by CELs corrected upwards to account for the possible presence of small temperature fluctuations within the nebulae. We note that the results of Esteban et al. (2005) show that some of the dispersion in these values of O/H (and in the corresponding values based on CELs) arises from the Galactic abundance gradient. The assumption of small temperature fluctuations might not be right for the PNe (Wesson et al. 2005). Besides, only IC 418 has measurements of suitable O I RLs (Sharpee et al. 2003). Hence, we derived their RLs oxygen abundances using the O⁺⁺ abundances implied by multiplet 1 of O II and the ionization fraction for this ion inferred from the CELs analysis.

Table 4. Ionic abundances from CELs and RLs: $X^{+i} = 12 + \log(X^{+i}/H^+)$

Object	Ar ⁺⁺	Cl ⁺⁺	N ⁺	Ne ⁺⁺	O ⁺	O ⁺⁺	He ⁺	He ⁺⁺	C ⁺⁺	O ⁺⁺
	CELs	CELs	CELs	CELs	CELs	CELs	RLs	RLs	RLs	RLs
O-rich dust PNe										
Cn 1-5	6.38±0.03	5.22±0.05	8.19 ^{+0.07} _{-0.03}	8.28±0.04	8.26 ^{+0.16} _{-0.04}	8.70±0.04	11.01±0.01	9.09	9.01
DdDm 1	5.61±0.04	4.59±0.04	6.75 ^{+0.08} _{-0.04}	7.19±0.06	7.38 ^{+0.20} _{-0.09}	7.87±0.04	10.94±0.02	8.39
H 1-50	5.99±0.03	4.88±0.04	7.01 ^{+0.06} _{-0.03}	7.94±0.04	7.38 ^{+0.13} _{-0.05}	8.64±0.05	11.00±0.01	10.04±0.02	8.35	9.09
M 1-42	6.27±0.03	5.04±0.04	7.89±0.04	8.03±0.04	7.64 ^{+0.07} _{-0.04}	8.39±0.04	11.20±0.01	10.04±0.02	9.39	9.63
M 2-27	6.50±0.03	5.29 ^{+0.06} _{-0.02}	7.66±0.07	8.37±0.04	7.64 ^{+0.17} _{-0.10}	8.84±0.04	11.15±0.01	8.84±0.02	8.85	9.27
M 2-31	6.15±0.04	5.00±0.04	7.04±0.05	8.06±0.04	7.24 ^{+0.12} _{-0.06}	8.64±0.05	11.07±0.01
M 2-42	6.16±0.03	5.14±0.07	7.00 ^{+0.07} _{-0.03}	8.04±0.04	7.33 ^{+0.17} _{-0.06}	8.73±0.04	11.06±0.01	8.45±0.08
MyCn 18	6.33±0.03	5.31±0.03	7.57±0.04	8.18±0.05	7.68 ^{+0.09} _{-0.06}	8.53±0.04	11.00±0.02	8.66±0.02	8.36	8.87
NGC 3132	6.38±0.03	5.18±0.03	8.19±0.04	8.30±0.04	8.47±0.06	8.53±0.05	11.05±0.01	9.52±0.02	8.83	8.81
NGC 6210	5.93±0.04	4.70±0.05	6.47±0.05	8.12±0.06	7.09±0.10	8.55±0.06	11.02±0.02	9.28±0.02	8.80	8.97
NGC 6439	6.35±0.03	5.12±0.03	7.52±0.05	8.16±0.04	7.67±0.07	8.60±0.04	11.05±0.02	10.31±0.02	8.99	9.06
NGC 6543	6.48±0.03	5.22±0.06	6.80 ^{+0.10} _{-0.05}	8.24±0.05	7.20 ^{+0.20} _{-0.06}	8.79±0.05	11.06±0.01	8.77	9.07
NGC 7026	6.22±0.02	5.16 ^{+0.06} _{-0.02}	7.56 ^{+0.08} _{-0.04}	8.19±0.03	7.66 ^{+0.22} _{-0.06}	8.64±0.03	11.03±0.01	10.11±0.02	8.94	9.07
C-rich dust PNe										
Hu 2-1	5.69±0.03	4.51 ^{+0.07} _{-0.03}	6.93 ^{+0.16} _{-0.04}	7.44±0.04	7.50 ^{+0.42} _{-0.11}	8.23 ^{+0.07} _{-0.04}	10.91±0.01	8.39±0.02	8.62	8.71
IC 418	6.00±0.03	4.82±0.04	7.63±0.06	6.78±0.04	8.34 ^{+0.11} _{-0.15}	8.09±0.04	10.96±0.01	8.74	8.24
M 1-20	5.77±0.03	4.65 ^{+0.12} _{-0.06}	6.79 ^{+0.11} _{-0.05}	7.69±0.04	7.34 ^{+0.28} _{-0.10}	8.55±0.05	10.99±0.01	7.60 ^{+0.10} _{-0.16}	8.67	8.66
NGC 40	5.67±0.02	4.65±0.03	7.94±0.04	5.80±0.03	8.65±0.06	7.11±0.03	10.78±0.01	7.56 ^{+0.13} _{-0.16}	8.81	8.33
NGC 3242	5.60±0.03	4.40±0.03	5.55±0.04	7.88±0.04	6.50±0.06	8.43±0.05	10.87±0.02	10.34±0.02	8.79	8.84
NGC 3918	5.93±0.03	4.71±0.04	7.15±0.05	7.88±0.04	7.66 ^{+0.09} _{-0.06}	8.45±0.05	10.82±0.02	10.55±0.02	8.70	8.82
NGC 6826	6.06±0.02	4.85±0.03	6.22±0.06	7.88±0.03	7.00±0.08	8.55±0.04	11.00±0.01	7.34 ^{+0.10} _{-0.16}	8.74	8.82
H II regions										
M8	6.16±0.02	5.04±0.03	7.54±0.03	7.05±0.04	8.37 ^{+0.12} _{-0.04}	7.89±0.03	10.84±0.01	8.31	8.24
M16	6.19±0.04	5.09±0.04	7.73±0.03	7.15±0.05	8.47±0.05	7.92±0.04	10.90±0.01	8.39	8.31
M17	6.30±0.03	5.06±0.03	6.84±0.04	7.76±0.03	7.80 ^{+0.07} _{-0.04}	8.45±0.03	10.98±0.01	8.73	8.72
M20	6.16±0.02	5.04±0.03	7.59±0.04	6.68±0.03	8.48±0.05	7.73±0.02	10.85±0.01	8.19	8.18
M42	6.33±0.03	5.12±0.04	6.87±0.04	7.77±0.03	7.71 ^{+0.10} _{-0.05}	8.43±0.05	10.98±0.01	8.35	8.61
NGC 3576	6.30±0.05	4.94±0.03	7.06±0.04	7.70±0.02	8.11±0.06	8.37±0.01	10.97±0.01	8.44	8.67
NGC 3603	6.29±0.02	5.04±0.04	6.48±0.06	7.78±0.03	7.34 ^{+0.12} _{-0.06}	8.44±0.03	11.00±0.01	8.49	8.71

The final abundances for each PN and H II region are listed in Table 5.

3.4 Uncertainties

The uncertainties in the physical conditions and the ionic abundances are computed through a Monte Carlo simulation. We generate 200 random values for each line intensity using a Gaussian distribution centred in the observed line intensity and with a sigma equal to the associated uncertainty. For higher number of Monte Carlo simulations, the errors in the computed quantities remain the same.

We derive the values of T_e , n_e , and the ionic abundances for every Monte Carlo run and calculate the errors associated with each quantity from the 16 and 84 percentiles; these values define a confidence interval of 68 per cent which is equivalent to one standard deviation in a Gaussian distribution. We assign a typical uncertainty of 5% and 15% to the C⁺⁺ and O⁺⁺ ionic abundances, respectively, computed from RLs. We use this simplified approach because the determination of uncertainties for the O⁺⁺ abundances implied by RLs is difficult and unreliable, and the C⁺⁺ abundances are only used to calculate the C/O abundance ratio from the ratio C⁺⁺/O⁺⁺.

Some of the O II lines from multiplet 1 are not observed and we have to estimate their contribution to the multiplet, which can depend on the electron density. In addition, some of the O II lines could be blended with nearby weaker lines. An uncertainty of 15% corresponds to the typical difference between the abundances derived from individual lines of multiplet 1 and from the total intensity of the multiplet and also to the differences with the O⁺⁺ computed with other multiplets (García-Rojas et al. 2013; Liu et al. 2004b). A complete analysis of the uncertainties related to the O⁺⁺ abundances implied by RLs should also take into account the information provided by the other multiplets and would be rather onerous. We consider that our simple approach is sufficient for the purposes of this paper. The uncertainty of 5% for the C⁺⁺ abundances arises from the typical uncertainty of the intensity of C II 4267 relative to H β in our sample objects.

As for the total abundances, we consider not only the uncertainties associated with the physical conditions and the ionic abundances but also those related to the adopted ICF. To estimate the uncertainties associated with the ICFs we perform another Monte Carlo simulation. We construct a uniform distribution for each ICF, where the central value is the ICF calculated from the observed degree of ionization, and the minimum and maximum values are ob-

Table 5. Abundance ratios: $\{X/H\} = 12 + \log(X/H)$

Object	{Ar/H}	{Cl/H}	{N/H} [*]	{Ne/H}	{O/H}	{He/H}	log(C/O)	{O/H}	Galactic
	CELs	CELs	CELs	CELs	CELs	RLs	RLs	RLs	component
O-rich dust PNe									
Cn 1-5	6.45 ^{+0.13} _{-0.27}	5.35±0.08	8.77 ^{+0.12} _{-0.24}	8.66 ^{+0.09} _{-0.04}	8.84 ^{+0.06} _{-0.02}	11.10±0.01	0.02 ^{+0.33} _{-0.38}	9.14	bulge
DdDm 1	5.69 ^{+0.14} _{-0.32}	4.73 ^{+0.04} _{-0.10}	7.36 ^{+0.11} _{-0.25}	7.55±0.07	7.99 ^{+0.07} _{-0.03}	10.94±0.02	8.51	halo
H 1-50	6.22 ^{+0.47} _{-0.24}	5.18 ^{+0.18} _{-0.12}	8.32 ^{+0.11} _{-0.27}	7.96 ^{+0.03} _{-0.07}	8.69±0.04	11.04±0.01	-0.68±0.38	9.14	bulge
M 1-42	6.42 ^{+0.15} _{-0.28}	5.23 ^{+0.03} _{-0.10}	8.73 ^{+0.15} _{-0.22}	8.05±0.07	8.48±0.04	11.22±0.01	-0.24 ^{+0.36} _{-0.40}	9.72	bulge
M 2-27	6.69 ^{+0.19} _{-0.23}	5.56 ^{+0.11} _{-0.09}	8.89 ^{+0.14} _{-0.23}	8.54±0.06	8.87 ^{+0.06} _{-0.03}	11.16±0.01	-0.37±0.38	9.30	bulge
M 2-31	6.36 ^{+0.58} _{-0.08}	5.31 ^{+0.26} _{-0.10}	8.46 ^{+0.15} _{-0.24}	8.20±0.06	8.66±0.04	11.07±0.01	bulge
M 2-42	6.37 ^{+0.56} _{-0.16}	5.45 ^{+0.24} _{-0.12}	8.41 ^{+0.15} _{-0.23}	8.18±0.05	8.74±0.04	11.06±0.01	9.50	bulge
MyCn 18	6.47 ^{+0.15} _{-0.32}	5.50 ^{+0.03} _{-0.11}	8.48 ^{+0.14} _{-0.24}	8.41±0.06	8.58±0.04	11.00±0.01	-0.49±0.37	8.93	disc
NGC 3132	6.40 ^{+0.14} _{-0.27}	5.30 ^{+0.04} _{-0.10}	8.53 ^{+0.14} _{-0.20}	8.36±0.06	8.81±0.03	11.06±0.01	-0.13±0.34	9.08	disc
NGC 6210	6.15 ^{+0.59} _{-0.10}	5.02 ^{+0.26} _{-0.06}	7.95 ^{+0.15} _{-0.24}	8.16±0.07	8.57±0.05	11.02±0.02	-0.10 ^{+0.39} _{-0.33}	8.99	disc
NGC 6439	6.55 ^{+0.14} _{-0.25}	5.37 ^{+0.04} _{-0.10}	8.54 ^{+0.15} _{-0.27}	8.20±0.05	8.69±0.05	11.12±0.02	-0.05±	9.15	bulge
NGC 6543	6.70 ^{+0.60} _{-0.08}	5.57 ^{+0.26} _{-0.11}	8.40 ^{+0.13} _{-0.25}	8.36±0.07	8.80 ^{+0.06} _{-0.03}	11.06±0.02	-0.23 ^{+0.40} _{-0.36}	9.08	disc
NGC 7026	6.42 ^{+0.12} _{-0.34}	5.41 ^{+0.05} _{-0.09}	8.62 ^{+0.13} _{-0.31}	8.22±0.05	8.71 ^{+0.06} _{-0.02}	11.08±0.01	-0.10 ^{+0.34} _{-0.38}	9.14	disc
C-rich dust PNe									
Hu 2-1	5.81 ^{+0.14} _{-0.31}	4.68 ^{+0.05} _{-0.10}	7.73±0.16	7.71 ^{+0.20} _{-0.04}	8.30 ^{+0.14} _{-0.03}	10.91±0.01	-0.09 ^{+0.32} _{-0.39}	8.78	disc
IC 418	6.05 ^{+0.16} _{-0.32}	4.94 ^{+0.04} _{-0.11}	7.82 ^{+0.16} _{-0.11}	7.54 ^{+0.05} _{-0.12}	8.54±0.09	10.96±0.01	0.25 ^{+0.31} _{-0.34}	8.69	disc
M 1-20	5.96 ^{+0.21} _{-0.27}	4.92 ^{+0.11} _{-0.12}	8.03 ^{+0.13} _{-0.16}	7.85 ^{+0.11} _{-0.05}	8.58 ^{+0.06} _{-0.03}	10.99±0.01	0.06 ^{+0.33} _{-0.37}	8.68	bulge
NGC 40	6.17 ^{+0.14} _{-0.63}	4.92 ^{+0.05} _{-0.10}	7.96 ^{+0.15} _{-0.11}	7.60 ^{+0.52} _{-0.15}	8.66±0.05	>10.78	-0.48 ^{+0.33} _{-0.56}	9.89	disc
NGC 3242	5.91 ^{+0.61} _{-0.06}	4.89 ^{+0.25} _{-0.12}	7.56 ^{+0.15} _{-0.12}	7.95 ^{+0.04} _{-0.08}	8.50±0.06	10.98±0.01	0.03 ^{+0.45} _{-0.34}	8.91	disc
NGC 3918	6.18 ^{+0.15} _{-0.36}	5.01 ^{+0.05} _{-0.10}	8.13±0.14	8.00±0.08	8.63±0.06	11.01±0.01	-0.12±0.36	9.01	disc
NGC 6826	6.28 ^{+0.60} _{-0.05}	5.19 ^{+0.26} _{-0.09}	7.78 ^{+0.16} _{-0.10}	8.01±0.06	8.56 ^{+0.03} _{-0.02}	11.00±0.01	-0.01 ^{+0.39} _{-0.36}	8.83	disc
H II regions									
M8	6.25 ^{+0.16} _{-0.31}	5.18 ^{+0.06} _{-0.09}	7.67 ^{+0.16} _{-0.11}	7.65 ^{+0.09} _{-0.05}	8.50 ^{+0.10} _{-0.03}	>10.84	-0.27±0.30	8.71	disc
M16	6.30 ^{+0.14} _{-0.25}	5.24 ^{+0.05} _{-0.11}	7.84 ^{+0.18} _{-0.11}	7.81±0.05	8.58±0.04	>10.90	-0.29±0.33	8.80	disc
M17	6.41 ^{+0.15} _{-0.34}	5.22 ^{+0.05} _{-0.09}	7.58±0.13	7.85±0.05	8.54±0.03	10.98±0.01	-0.01 ^{+0.36} _{-0.33}	8.76	disc
M20	6.32 ^{+0.15} _{-0.31}	5.21 ^{+0.04} _{-0.10}	7.66 ^{+0.15} _{-0.11}	7.50±0.06	8.55±0.04	>10.85	-0.47 ^{+0.34} _{-0.29}	8.71	disc
M42	6.46 ^{+0.16} _{-0.29}	5.29 ^{+0.04} _{-0.10}	7.68 ^{+0.15} _{-0.10}	7.84±0.05	8.51±0.05	10.98±0.01	-0.26 ^{+0.36} _{-0.33}	8.65	disc
NGC 3576	6.34 ^{+0.13} _{-0.30}	5.06 ^{+0.04} _{-0.10}	7.51 ^{+0.15} _{-0.08}	7.89±0.05	8.56±0.03	10.97±0.01	-0.33±0.34	8.74	disc
NGC 3603	6.47 ^{+0.14} _{-0.30}	5.28 ^{+0.05} _{-0.11}	7.60±0.13	7.82±0.05	8.47±0.03	11.00±0.01	0.20 ^{+0.34} _{-0.30}	8.72	disc

^{*} N/H computed from N/O = N⁺/O⁺.

tained from the uncertainties associated with each ICF provided in Delgado-Inglada et al. (2014). From this distribution we generate random values that we use to calculate the total abundances for the 200 runs. The errors associated with the abundance of each element are given by the 16 and 84 percentiles. Our computed uncertainties in the total abundances are probably overestimated since we are using the maximum dispersion in each ICF, created by a large grid of photoionization models, whereas real nebulae are probably better represented by a smaller set of models.

In the case of nitrogen, we use the method described above when using the ICF from Delgado-Inglada et al. (2014), and we adopt a uniform distribution of errors of ±0.2 dex when using N/O = N⁺/O⁺, which seems reasonable given the dispersion we get for abundance ratios like N/O and N/Cl in the sample H II regions.

As for He, Delgado-Inglada et al. (2014) proposed that one should compute the total He abundance by adding the contributions of He⁺ and He⁺⁺, including the contribution of He⁰ in the uncertainties associated with He/H. There are four objects in the sample (three H II regions and one PN) with a very low degree of ionization, where the abundance of He⁰ is important and thus, the value of He/H is very uncertain. We represent their He abundance

in the figures as a lower limit and we only plot the errors associated with the He ionic abundances and not with the ICF.

Each of the ICFs derived in Delgado-Inglada et al. (2014) is valid for a certain range in the degree of ionization, given by O⁺⁺/(O⁺+O⁺⁺) or He⁺⁺/(He⁺+He⁺⁺); outside this range the ICF formula is not necessarily correct. Here we use the ICFs from Delgado-Inglada et al. (2014) in all the objects, regardless of their degree of ionization, but we assign higher uncertainties in the ICFs when the objects fall outside the range of validity. The low dispersion found in some of the abundance ratios, such as Ar/Cl, suggests that the adopted ICFs are still valid outside the ranges proposed in Delgado-Inglada et al. (2014), at least in some cases.

Since the ICFs for many elements are based on the O⁺⁺/(O⁺+O⁺⁺) ratio, the uncertainties introduced by these corrections are not independent. If we do not consider this effect, we get very large uncertainties for some of the abundance ratios considered below, namely, Ar/Cl and Ne/Cl. We have used the model results of Delgado-Inglada et al. (2014) to obtain better estimates of the uncertainties in those cases. The uncertainties in log(Ar/Cl) associated with the ICF are:

$$+0.30/ - 0.90 \text{ dex, for } O^{++}/(O^+ + O^{++}) < 0.05$$

+0.20/ - 0.15 dex, for $0.05 \leq O^{++}/(O^{+} + O^{++}) < 0.45$

+0.10/ - 0.04 dex, for $0.45 \leq O^{++}/(O^{+} + O^{++}) \leq 0.95$

+0.66/ - 0.01 dex, for $O^{++}/(O^{+} + O^{++}) > 0.95$.

As for the $\log(\text{Ne}/\text{Cl})$ values, the uncertainties associated with the ICF are:

+0.70/ - 1.30 dex, for $O^{++}/(O^{+} + O^{++}) < 0.1$

+0.13/ - 0.08 dex, for $0.1 \leq O^{++}/(O^{+} + O^{++}) \leq 0.95$

+0.20/ - 0.30 dex, for $O^{++}/(O^{+} + O^{++}) > 0.95$.

We do not include the uncertainties on the atomic data since it is very difficult to quantify them but we have selected the atomic data that we consider more reliable (see e.g. Stasińska et al. 2013).

The final adopted value for each parameter is the value computed from the observed intensities except for the electron density, for which we prefer the median of the distribution of average densities obtained from the available diagnostics in each run. In the low- and high-density limits, the median is less affected by the large variations obtained in the density values due to small variations in the intensity ratios. Note that the electron density is a special case; for some of the other calculated quantities, the use of the median would lead to similar results, for other quantities, such as the total abundances, it is not a good idea to use the median since their distributions depend on the distribution of the uncertainties due to the ICFs, for which we can only estimate the width, not the shape.

4 RESULTS AND DISCUSSION

4.1 Chlorine as a proxy for metallicity

We have derived the abundances of He, C, N, O, Ne, Cl, and Ar. From these elements, only Cl and Ar are not expected to be modified by the evolution of low and intermediate mass stars, and can be used to infer the metallicity of the PN progenitor star. We could also use S but, as we mentioned in Section 1, there are problems with the determination of the abundance of this element. Figure 1 shows the Ar/Cl abundance ratio as a function of Cl/H for the group of PNe and H II regions studied here. The small dots in the figure correspond to the values derived for each Monte Carlo run and take into account all the uncertainties arising from errors in the line fluxes involved in the calculations and those related to the adopted ICF. The metallicity of our objects changes by an order of magnitude, but all of them show $\log(\text{Ar}/\text{Cl}) \approx 1.1$ with very low dispersion. The average value of the Ar/Cl abundance ratio considering our whole sample of ionized nebulae is $\log(\text{Ar}/\text{Cl}) = 1.10 \pm 0.02$, where 0.02 is the standard error of the mean. The tight correlation between the Cl/H and the Ar/H values is in agreement with a lockstep evolution of both elements, at least for the metallicity range covered by our objects. Since the Ar and Cl abundances are very difficult to calculate in the interstellar medium (Jenkins 2009), in stars, and in the Solar System (Asplund et al. 2009), the results obtained from the analysis of photoionized nebulae provide the best estimates of the abundances of these two elements.

The uncertainties in the values of Ar/H are significantly higher than those found for Cl/H, as can be seen in Table 5. Hence, in what follows we use the Cl/H abundance ratio as a proxy for the metallicity of all the objects.

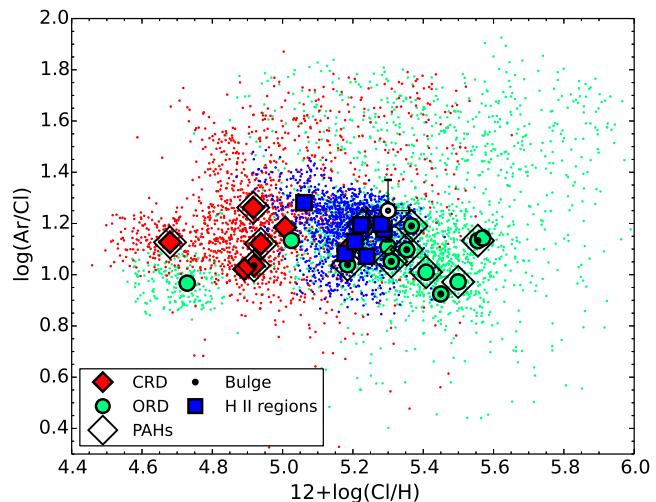


Figure 1. Values of Ar/Cl as a function of Cl/H. The green circles represent ORD PNe, the red diamonds CRD PNe, and the blue squares the H II regions. We mark with open diamonds the PNe with PAH emission and with a small black dot the PNe from the bulge. The coloured small dots correspond to the values obtained for the 200 Monte Carlo runs performed for each object. The protosolar abundances of Lodders (2010) are overplotted with the solar symbol. The CRD PN NGC 6826, with $12 + \log(\text{Cl}/\text{H}) = 5.19$ and $\log(\text{Ar}/\text{Cl}) = 1.09$, is hidden behind the H II regions.

4.2 Metallicity differences between H II regions and PNe with CRD and ORD

We also show in Figure 1 the protosolar abundances provided by Lodders (2010). Unfortunately, the Solar System abundances of these elements are not well constrained (Asplund et al. 2009). If we use the photospheric abundances provided by Asplund et al. (2009) for Ar and Cl, $12 + \log(\text{Ar}/\text{H}) = 6.40$ and $12 + \log(\text{Cl}/\text{H}) = 5.50$ with a correction of ~ 0.04 dex due to diffusion effects, we would get $12 + \log(\text{Cl}/\text{H}) = 5.54$ and $\log(\text{Ar}/\text{Cl}) = 0.9$ instead of the values favoured by Lodders (2010), $12 + \log(\text{Cl}/\text{H}) = 5.3$ and $\log(\text{Ar}/\text{Cl}) = 1.25$. However, it is clear from Figure 1 that most of the ORD PNe have abundances close to or above solar, H II region abundances are below solar, and CRD PNe show even lower abundances (note that NGC 6826, our more metal-rich CRD PN, with $12 + \log(\text{Ar}/\text{H}) = 6.28$ and $12 + \log(\text{Cl}/\text{H}) = 5.19$, is hidden behind the H II regions in this figure). It seems that the progenitors of the CRD PNe in our sample were formed in a subsolar metallicity medium, which agrees both with the expectation of a higher efficiency of the TDU at low metallicities (see e.g. Karakas & Lattanzio 2014) and with the observation of larger fractions of CRD PNe in the metal-poor environment of the Magellanic Clouds (Bernard-Salas et al. 2009). On the other hand, the progenitors of the ORD PNe were born in environments that cover our full metallicity range. In agreement with García-Hernández & Górný (2014), we find that PNe with dual chemistry (with both silicates and PAHs in their spectra) have metallicities close to solar.

Several ORD PNe (7 out of 13) belong to the bulge, where the average PN metallicity is known to be higher than in the disc (see e.g. Wang & Liu 2007). However, three of the disc PNe have higher values of Cl/H than the H II regions. Since all our disc objects are located roughly at the same range of Galactocentric distances, chemical evolution models predict that the PNe progenitor stars should have formed at lower metallicities than the ones traced by H II regions. Rodríguez & Delgado-Inglada (2011) obtained a

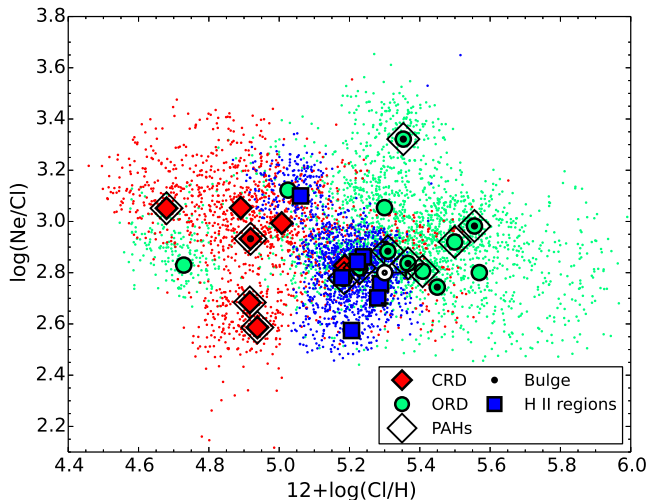


Figure 2. Values of Ne/Cl as a function of Cl/H. The protosolar abundances of Lodders (2010) are overplotted with the solar symbol. We use the same symbols as in Figure 1.

similar result from an analysis of the oxygen abundances in a group of PNe and H II regions belonging to the solar neighbourhood. Rodríguez & Delgado-Inglada (2011) speculated that this could be due to the presence of organic refractory dust grains in H II regions containing significant amounts of oxygen, but the fact that we find the same result for chlorine indicates that this is a more general effect. A possible explanation is stellar migration of the central stars (and the Sun?) from inner regions of the Galaxy, but other explanations, such as infall of metal-poor gas clouds into the Galaxy or changes in the stellar composition arising during star formation or stellar evolution cannot be ruled out at the moment. Six of the seven H II regions show similar metallicities, indicating that the interstellar medium in the solar neighbourhood is chemically well mixed. This is confirmed by the values we find for O/H for the seven H II regions (see Table 5 and Figure 3 below). The chlorine abundance of NGC 3576 is somewhat low, but compatible within the errors with the values of the other H II regions.

4.3 Inconclusive evidence for neon enrichment

Figure 2 shows the results for neon. Neon can be produced in stars with initial masses in the range $\sim 2\text{--}4 M_{\odot}$ (Karakas & Lattanzio 2003; Pignatari et al. 2013), and Milingo et al. (2010) argue that there is evidence for neon enrichment in some Galactic PNe. Our Ne/Cl abundance ratios show a large dispersion, and the fact that CRD PNe, H II regions, and ORD PNe cover similar ranges in Ne/Cl suggests that this dispersion arises from uncertainties in the ICF for neon. Our sample PNe do not show clear evidence for Ne enrichment, although we cannot rule it out since it could be masked by the uncertainties in the derived Ne/H abundance ratio. If we reject the high value of Ne/Cl in NGC 3576, since it could be due to the too low value found for Cl/H in this object, we can see that the other H II regions and several PNe cluster around the solar value of Ne/Cl. The remaining PNe might have some neon enrichment.

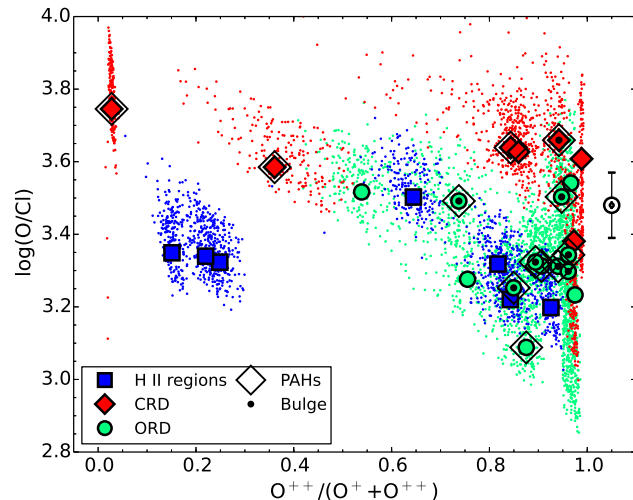


Figure 4. Values of O/Cl as a function of $O^{++}/(O^{+} + O^{++})$. The protosolar abundances of Lodders (2010) are overplotted with the solar symbol. We use the same symbols as in Figure 1.

4.4 Oxygen production in the PNe with CRD

Our results for the O/Cl abundance ratio as a function of O/H and Cl/H are presented in Figure 3. Note that the trend followed by the dots that show the results of our Montecarlo propagation of errors in the right panel of Figure 3 is caused by the correlation between the uncertainties in the values we derive for O/Cl and Cl/H. The trend is not present in our computed values for these abundance ratios. However, in order to check if the ICF used to calculate the O/Cl values is introducing a bias in our results, we plot in figure 4 the O/Cl abundance ratios as a function of the degree of ionization, given by $\omega = O^{++}/(O^{+} + O^{++})$, which is the parameter on which the ICF is based: $Cl/O = (Cl^{++}/O^{+})(4.1620 - 4.1622\omega^{0.21})^{0.75}$. We see that the adopted ICF does not seem to be introducing any kind of bias in our results. In particular, the CRD PNe cover the full range of values of ω and their O/Cl abundance ratios do not follow any trend with ω .

It can be seen in Figure 3 that the metallicities implied by the Cl and O abundances do not agree for all the objects. The Sun, the H II regions, and the ORD PNe show similar values of the O/Cl abundance ratio, in agreement within the errors. However, the CRD PNe have values of O/Cl which are clearly higher. The exception is NGC 6826, the CRD PN with the highest metallicity, according to its chlorine abundance. The straightforward explanation of this result is that the low-metallicity CRD PNe besides being C-rich are enriched in oxygen.

As we commented in Section 1, canonical AGB models like those of Karakas (2010) do not predict oxygen enrichment at the metallicities that characterize our sample PNe, but models with diffusive convective overshooting like those of Pignatari et al. (2013), predict that the ejecta of stars with initial masses of $\sim 2\text{--}3 M_{\odot}$ and metallicities $Z = 0.01$ and 0.02 will be enriched in both C and O (with $C/O > 1$), with an increase in the O/H abundance ratio of up to ~ 0.26 dex. This agrees with the differences we find in the average values of $\log(O/Cl)$ for our objects: $\log(O/Cl) = 3.65 \pm 0.06$ for the CRD PNe excluding NGC 6826, 3.34 ± 0.13 for the ORD PNe, and 3.32 ± 0.09 for the H II regions. The fact that the CRD PN with the highest metallicity, NGC 6826, has a value of O/Cl similar to the ones found for ORD PNe and H II regions suggests that O

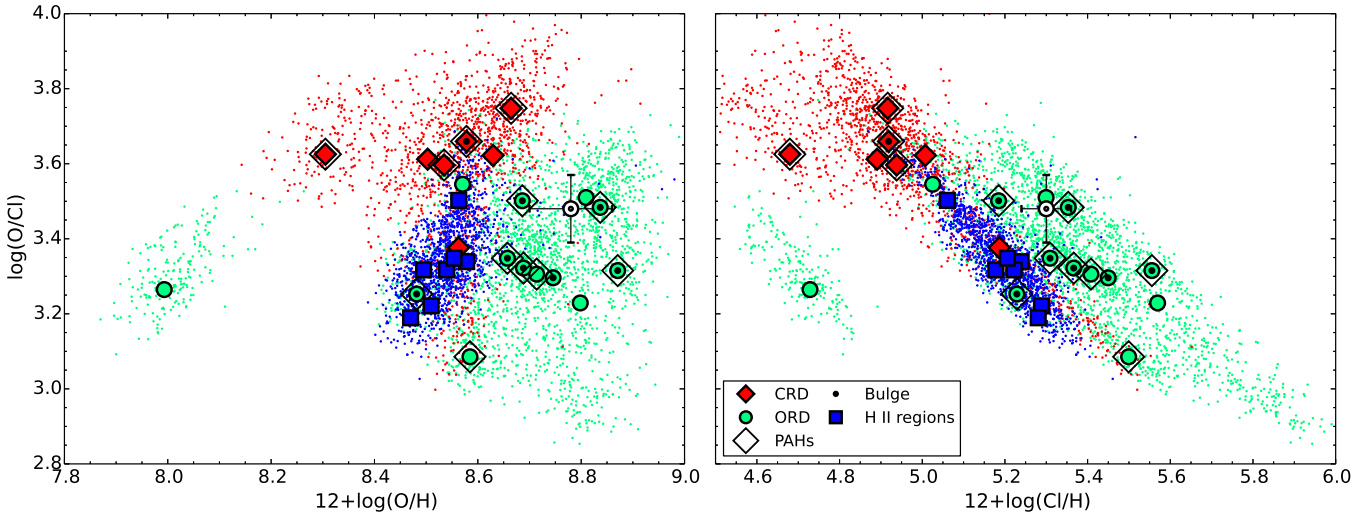


Figure 3. Values of O/Cl as a function of O/H (left panel) and Cl/H (right panel) for our sample of ORD PNe, CRD PNe, and H II regions. The protosolar abundances of Lodders (2010) are overplotted with the solar symbol. We use the same symbols as in Figure 1.

enrichment is no longer important at metallicities close to solar, but this should be confirmed by the analysis of other CRD PNe with similar metallicity. Note that NGC 6826 is suspected to have a binary companion (Méndez 1989), which might be responsible for its carbon enrichment.

We performed a rough estimation of the amount of oxygen produced by low-mass stars and high-mass stars using the yields calculated by Pignatari et al. (2013). To do this, we integrated the net yields over the Salpeter (1955) initial mass function in two mass ranges: 1.65–5 M_{\odot} and 15–60 M_{\odot} for $Z = 0.02$, 1.65–5 M_{\odot} and 15–25 M_{\odot} for $Z = 0.01$. We obtain that low-mass stars contribute about 4 per cent and about 10 per cent of the total oxygen produced by a single stellar population at $Z = 0.02$ and 0.01, respectively. These percentages are small, but they are likely to increase at lower metallicities, and detailed chemical evolution models will be needed to find out if low-mass stars are important producers of oxygen in different galaxies.

Figure 3 offers an explanation for the overabundance of oxygen in PNe of the solar neighbourhood found by Rodríguez & Delgado-Inglada (2011). This result would be due to a combination of two causes: the presence of high metallicity PNe in our vicinity for any of the reasons listed above plus oxygen enrichment in some of the lower metallicity PNe.

4.5 Nitrogen production in the PNe with CRD and ORD

Figure 5 shows the values of the N/O abundance ratio as a function of the helium abundance. This plot is commonly used to identify the descendants of massive progenitors, which are efficient producers of N and He according to the models of AGB evolution. The top panel of Figure 5 shows the results obtained using the ICFs of Delgado-Inglada et al. (2014). The H II regions show some dispersion in their values of N/O and we noted that it seems to be related to their degree of ionization, as measured with $O^{++}/(O^{+} + O^{++})$: the three H II regions of higher ionization have the largest values of N/O. We decided to compare the results with those obtained using the classical ICF for nitrogen: $N/O = N^{+}/O^{+}$. The middle panel of Figure 5 shows the abundances implied by this ICF. It can be seen that the new N/O ratios of the H II regions have less dispersion and a better agreement with the solar value. On the other hand, the val-

ues of N/O in the PNe with higher helium abundances now show a tight correlation with the helium abundance. We cannot think of any observational effect or bias that would introduce this correlation if it were not real, and we conclude that the classical ICF for nitrogen seems to be working better, at least for this sample of objects. The issue merits more investigation, but since our conclusions do not depend on the chosen ICF, we will not discuss this further.

The bottom panel of Figure 5 compares our results with the predictions of Karakas (2010) and Pignatari et al. (2013). The sequence of triangles with increasing size correspond to models with initial metallicities of $Z = 0.008$ and 0.02 and masses of 1, 1.25, 1.5, 1.75, 1.9, 2, 2.25, 2.5, 3, 3.5, 4, 4.5, 5, 5.5, 6, and 6.5 M_{\odot} (the sequence ends at 6 M_{\odot} for $Z = 0.008$) computed by Karakas (2010). The sequence of hexagons correspond to the models of Pignatari et al. (2013) with initial masses of 1.65, 2, 3, and 5 M_{\odot} and $Z = 0.01$ and 0.02. According to the models, most of our ORD PNe descend from stars with masses above 4.5 M_{\odot} , born in a medium of near-solar composition, whereas the CRD PNe would descend from stars with masses below $\sim 4 M_{\odot}$ formed in an environment with sub-solar metallicity. Note however, that extra mixing processes, stellar rotation, or the effect of a binary companion could produce large N/O ratios in PNe with initial masses not that high (Karakas 2010; Stasińska et al. 2013). In particular, the models we are considering imply that all but one of the bulge PNe have high-mass progenitors, as discussed by other authors (see e.g. Wang & Liu 2007; García-Hernández & Górný 2014). However, this conclusion should be considered with caution. Buell (2013) argues that if the bulge PNe had progenitor masses above 4 M_{\odot} , we would observe in the bulge bright carbon stars arising from stars of 2–4 M_{\odot} , which is not the case. Following the suggestion of Nataf & Gould (2012) that there is a population of helium-enhanced stars in the bulge, similar to those found in some globular clusters, Buell (2013) constructs a set of AGB models with masses between 1.2 and 1.8 M_{\odot} , $Z \sim 0.02$, and pre-enriched in helium, finding that they can reproduce the observed abundance ratios.

Since chlorine is a better proxy for the metallicity than oxygen, we display in Figure 6 the results for the nitrogen abundances relative to chlorine. We also show the predictions from the nucleosynthesis models of Karakas (2010) and Pignatari et al. (2013). As expected, the results for the ORD PNe are almost the same when

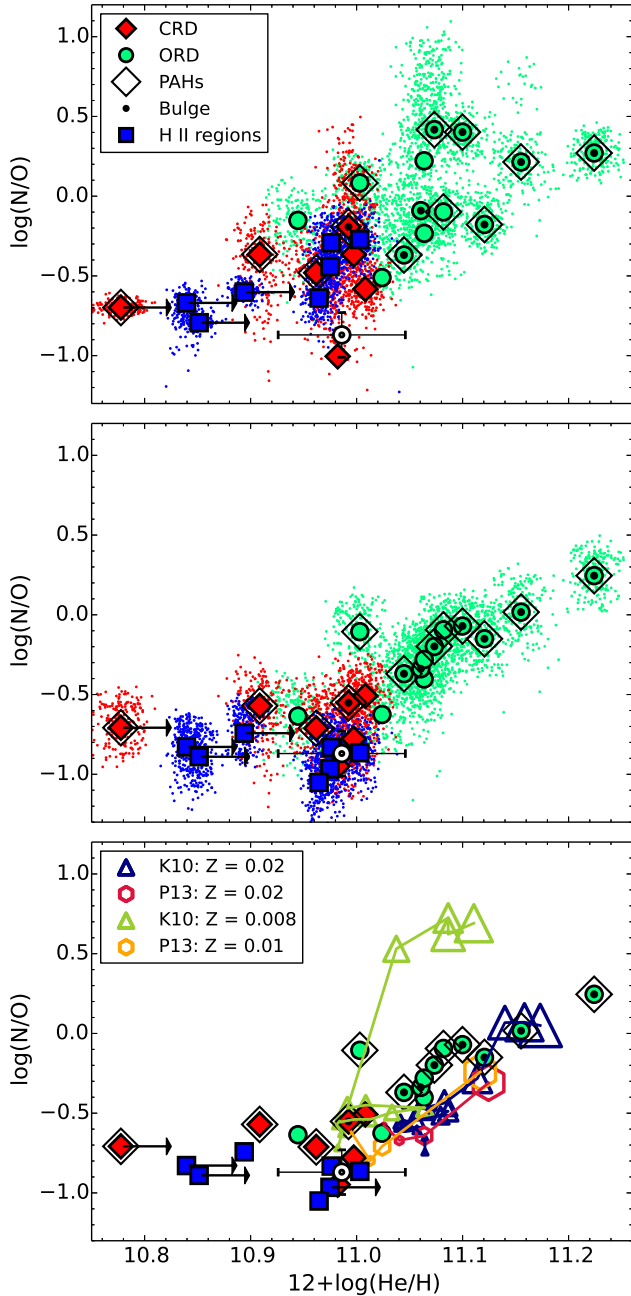


Figure 5. Values of N/O as a function of He/H. The protosolar abundances of Lodders (2010) are overplotted with the solar symbol. We use the same symbols as in Figure 1. We draw upper limits in the He abundance of four objects where the contribution of neutral helium is significant. The top panel shows the nitrogen abundances derived with the ICFs of Delgado-Inglada et al. (2014); in the middle panel the nitrogen abundances have been calculated using the classical ICF, $N/O = N^+/O^+$. The bottom panel shows the predictions from the nucleosynthesis models by Karakas (2010) and Pignatari et al. (2013) overplotted for comparison with the results of the middle panel. The size of the symbols is larger for higher mass progenitors (see the text for more information).

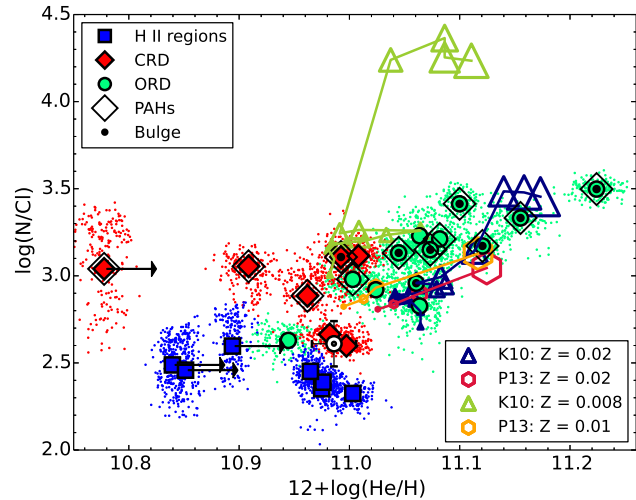


Figure 6. Values of N/Cl as a function of He/H. The N abundances have been calculated using the classical ICF, $N/O = N^+/O^+$. The protosolar abundances of Lodders (2010) are overplotted with the solar symbol. We use the same symbols as in Figure 5. We draw upper limits in the He abundance of four objects where the contribution of neutral helium is significant.

compared to the values in H II regions because their oxygen abundance has not been modified, but the N/Cl values obtained in the CRD PNe reveal that most of them are also significantly enriched in nitrogen.

4.6 The C/O abundance ratio

Figure 7 shows the C/O values as a function of He/H, both derived from RLs. For three of the ORD we do not have an estimate of the C/O abundance ratio and they do not appear in this figure. In principle, RLs and CELs might be tracing different nebular phases (see e.g. Liu et al. 2004b), but the values of C/O derived using RLs and CELs are similar in most cases (Liu et al. 2004b; Delgado-Inglada & Rodríguez 2014).

We can see that the value derived for C/O does not provide a direct indication of the type of dust grains present in a PN. This can be attributed to the uncertainties involved in its determination, since the C/O value is based on weak RLs and requires an ICF. In fact, the dispersion of our Monte Carlo error simulations shows that H II regions and ORD PNe have C/O values compatible with the expectation that $C/O < 1$ in these objects and the values of CRD PNe are also compatible with $C/O > 1$, as expected from their dust features. The average value of C/O for CRD PNe is also higher than the one shown by the other objects, which cluster around the solar value. Another effect that could affect the observed value of C/O is depletion of carbon or oxygen into dust grains. For these reasons, the dust features observed in the infrared spectra are likely to provide more reliable information on whether the value of C/O is below or above 1 in each object.

If we now examine the values of He/H (including those listed in Table 5 for the three ORD PNe that have no estimate of C/O), we can see that excluding the low-metallicity object from the halo, the ORD PNe have helium abundances which are systematically higher than those found for CRD PNe and H II regions. This is consistent with our conclusions above that they had massive (or pre-enriched) stellar progenitors, since AGB models predict that

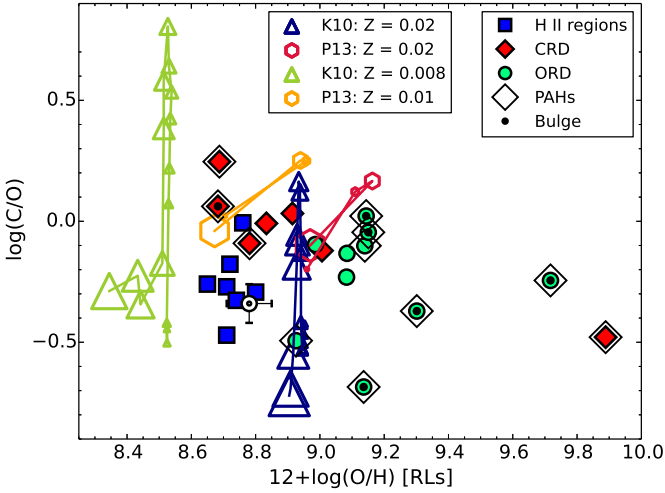


Figure 8. Values of C/O as a function of O/H derived from RLs for the studied PNe and the H II regions. The protosolar abundances of Lodders (2010) are overplotted with the solar symbol. We use the same symbols as in Figure 5. Note that for three of the ORD PNe we could not estimate the value of C/O and these objects are not plotted in this figure.

helium enrichment takes place for the stars with the highest masses. This is illustrated in the right panel of the figure, where we plot the same models we used for Figure 5.

In Figure 8, we also show the derived values of C/O but now as a function of the oxygen abundances implied by RLs (listed in Table 5). Since the correct values for the nebular oxygen abundances are likely to be intermediate between the ones implied by CELs and RLs (or close to either one), the O/H values derived from RLs complete our picture of the distribution in metallicity of the sample objects and their comparison with the Sun. The O/H values for H II regions and ORD PNe should be corrected upward by 0.10–0.15 dex to take into account the presence of oxygen in silicates and oxides within dust grains (Whittet 2010; Peimbert & Peimbert 2010). With this correction, the oxygen abundance in the H II regions would still be below solar for the results based on CELs, but would agree both with the solar abundance and with the abundances found for nearby B stars (Nieva & Przybilla 2012) for the results based on RLs. On the other hand, the oxygen abundances derived with CELs imply that the ORD PNe of the solar neighbourhood have a chemical composition which is close to solar, whereas RLs imply that these objects are significantly more metal-rich than the Sun. Both RLs and CELs imply that several nearby PNe are more metal-rich than the H II regions, a result confirmed by the derived values of C/H.

Figure 8 also shows the predictions of the AGB models of Karakas (2010) and Pignatari et al. (2013). In both sets of models the results for the lower mass objects indicate the initial values of O/H. As we commented above, the models of Karakas (2010) for the most massive stars with $Z = 0.008$ predict significant oxygen destruction, whereas the models of Pignatari et al. (2013) with initial masses of $2\text{--}3 M_{\odot}$ are enriched both in carbon and oxygen. As discussed above, our results for the CRD PNe agree with the predictions of Pignatari et al. (2013), at least for $Z = 0.01$. An extended analysis of other CRD PNe might provide more information.

5 CONCLUSIONS

We have studied the chemical composition of 20 Galactic PNe with high quality infrared and optical spectra. The sample includes one halo PN, eight bulge PNe, and eleven disc PNe. We have also selected from the literature seven H II regions from the solar neighbourhood with the best available optical spectra. Using the infrared dust features we have classified the PNe in two groups: PNe with ORD and PNe with CRD. The first ones show amorphous and/or crystalline silicates in their spectra whereas the second ones show the broad features at 11 and/or $30 \mu\text{m}$ associated with SiC and MgS.

We have computed the physical conditions and the chemical abundances following the same procedure in all the objects. The abundances derived here are based on the best available ICFs, mainly those derived by Delgado-Inglada et al. (2014), and the uncertainties in the element abundances include the uncertainties introduced by the physical conditions, the ionic abundances, and the ICFs.

We find a tight correlation between the abundances of Cl and Ar, in agreement with a lockstep evolution of both elements. The metallicity in our sample, traced by Cl/H, covers one order of magnitude, and there are significant differences in the Cl/H ratio among the three groups of objects studied here. In general, the PNe with CRD have low metallicity, the H II regions have intermediate metallicities, and the PNe with ORD cover the whole range of metallicity (with some of them showing the highest abundances, even higher than the solar ones). This result indicates that the progenitors of the PNe with CRD were formed in a sub-solar metallicity medium (with the exception of NGC 6826, with a value of Cl/H similar to the H II regions) whereas most of the PNe with ORD were formed in a near-solar metallicity medium (with the exception of the halo PN DdDm 1).

The neon abundances at a given metallicity show a relatively large dispersion. The dispersion could be due to uncertainties in the ICF but we cannot rule out that some of the PNe are neon enriched.

The oxygen abundances do not always trace the metallicities of the objects. The O/Cl values in the Sun, the PNe with ORD, and the H II regions are similar, but most of the PNe with CRD show O/Cl values that are higher by a factor of two. The exception is NGC 6826, the CRD PN with higher metallicity in our sample. As we mentioned above, the progenitors of most of the PNe with ORD were formed in an environment with near-solar metallicity, where the nucleosynthesis process that can change the initial oxygen abundance are less efficient. This is in agreement with the similar values of O/Cl found in these PNe and in the H II regions. The low Cl/H abundances and the high O/Cl values found in all but one of the PNe with CRD provide evidence of oxygen production in the progenitor stars of PNe with CRD. Non-standard nucleosynthesis models, such as those by Pignatari et al. (2013), that include an extra mixing mechanism, predict a significant production of oxygen via the third dredge-up in stars with masses around $\sim 2\text{--}3 M_{\odot}$, explaining our results. The relevance for galactic chemical evolution of oxygen production in low mass stars deserves further study using chemical evolution models.

The comparison of the He/H, C/O, and N/O abundance ratios derived for the PNe with the predictions of nucleosynthesis models, suggests that the PNe with CRD descend from stars with masses in the range $1.5\text{--}3 M_{\odot}$ whereas the PNe with ORD and the highest abundances of nitrogen and helium would arise from stars with higher initial masses. The theoretical models indicate that they descend from stars with masses $\gtrsim 4.5 M_{\odot}$, but this limit would be

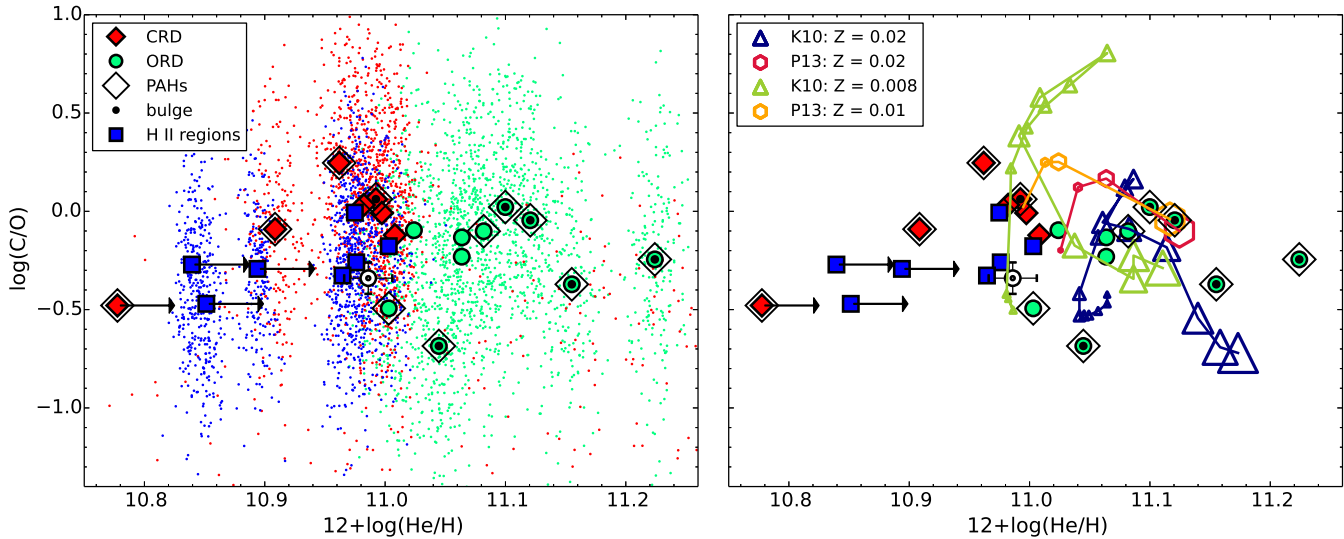


Figure 7. Values of C/O as a function of He/H for the studied PNe and the H II regions. The protosolar abundances of Lodders (2010) are overplotted with the solar symbol. We use the same symbols as in Figure 1. Note that for three of the ORD PNe we could not estimate the value of C/O and these objects are not plotted in this figure.

smaller with models that include stellar rotation, extra mixing processes or pre-enrichment.

Our results indicate that Ar and Cl are the best metallicity indicators for PNe. At any metallicity their abundances reflect the composition of the interstellar medium where the PN progenitors were formed. Moreover, the ICFs adopted here for Ar and Cl can be used when only Cl^{++} and Ar^{++} lines are observed, making easier a homogeneous calculation of PN metallicities. High resolution and deep spectra are needed, especially of extragalactic PNe, to delve in this issue and calculate, for example, metallicity gradients using Cl or Ar. Besides, the obtention of high quality optical spectra in which we can measure Cl and Ar lines will provide more reliable estimates of the electron densities. The observed extragalactic PNe are often the brightest ones, with high electron densities, where the commonly used density diagnostic ratio based on [S II] lines is not sensitive.

ACKNOWLEDGEMENTS

We are grateful to the anonymous referee for valuable comments and suggestions. The authors thank L. Carigi, L. Hernández-Martínez, and M. Pignatari for fruitful discussions and comments. G.D.-I. gratefully acknowledges a DGAPA postdoctoral grant from the Universidad Nacional Autónoma de México (UNAM). C.M. and G.S. acknowledge support from the following Mexican projects: CB-2010/153985, PAPIIT-IN105511, and PAPIIT-IN112911. M.P. is grateful for the financial support provided by CONACyT grant 129753. M.R. and G.D.-I. acknowledge support from Mexican CONACyT grant CB-2009-01/131610. This work has made use of NASA's Astrophysics Data System, and the SIMBAD database operated at CDS, Strasbourg, France.

REFERENCES

- Allende Prieto C., Lambert D. L., Asplund M., 2002, *ApJ*, 573, L137
- Asplund M., Grevesse N., Sauval A. J., Scott P., 2009, *ARA&A*, 47, 481
- Barker T., Cudworth K. M., 1984, *ApJ*, 278, 610
- Bernard-Salas J., Peeters E., Sloan G. C., Gutenkunst S., Matsuura M., Tielens A. G. G. M., Zijlstra A. A., Houck J. R., 2009, *ApJ*, 699, 1541
- Buell J. F., 2013, *MNRAS*, 428, 2577
- Ciardullo R., Bond H. E., Sipior M. S., Fullton L. K., Zhang C.-Y., Schaefer K. G., 1999, *AJ*, 118, 488
- Clegg R. E. S., Peimbert M., Torres-Peimbert S., 1987, *MNRAS*, 224, 761
- Davey A. R., Storey P. J., Kisielius R., 2000, *A&AS*, 142, 85
- Delgado-Inglada G., Morisset C., Stasińska G., 2014, *MNRAS*, 440, 536
- Delgado-Inglada G., Rodríguez M., 2014, *ApJ*, 784, 173
- Depew K., Parker Q. A., Miszalski B., De Marco O., Frew D. J., Acker A., Kovacevic A. V., Sharp R. G., 2011, *MNRAS*, 414, 2812
- Esteban C., García-Rojas J., Peimbert M., Peimbert A., Ruiz M. T., Rodríguez M., Carigi L., 2005, *ApJ*, 618, L95
- Esteban C., Peimbert M., García-Rojas J., Ruiz M. T., Peimbert A., Rodríguez M., 2004, *MNRAS*, 355, 229
- Galavís M. E., Mendoza C., Zeppen C. J., 1997, *A&AS*, 123, 159
- García-Hernández D. A., Górný S. K., 2014, *A&A*, 567, A12
- García-Rojas J., Esteban C., Peimbert A., Rodríguez M., Peimbert M., Ruiz M. T., 2007, *Rev. Mex. Astron. Astrofis.*, 43, 3
- García-Rojas J., Esteban C., Peimbert M., Rodríguez M., Ruiz M. T., Peimbert A., 2004, *ApJS*, 153, 501
- García-Rojas J., Esteban C., Peimbert M., Costado M. T., Rodríguez M., Peimbert A., Ruiz M. T., 2006, *MNRAS*, 368, 253
- García-Rojas J., Peña M., Morisset C., Delgado-Inglada G., Mesa-Delgado A., Ruiz M. T., 2013, *A&A*, 558, A122
- Górný S. K., Chiappini C., Stasińska G., Cuisinier F., 2009, *A&A*, 500, 1089
- Górný S. K., Stasińska G., Escudero A. V., Costa R. D. D., 2004, *A&A*, 427, 231
- Henry R. B. C., Kwitter K. B., Balick B., 2004, *AJ*, 127, 2284
- Henry R. B. C., Kwitter K. B., Dufour R. J., Skinner J. N., 2008,

- ApJ, 680, 1162
- Herwig F., Bloeker T., Schoenberner D., El Eid, M., 1997, A&A, 324, L81
- Izotov Y. I., Stasińska G., Meynet G., Guseva N. G., Thuan T. X., 2006, A&A, 448, 955
- Jenkins E. B., 2009, ApJ, 700, 1299
- Karakas A. I., 2010, MNRAS, 403, 1413
- Karakas A. I., Lattanzio J. C., 2003, PASA, 20, 393
- Karakas A. I., Lattanzio J. C., 2014, preprint (arXiv: 1405.0062)
- Kingsburgh R. L., Barlow M. J., 1994, MNRAS, 271, 257
- Kisielius R., Storey P. J., Ferland G. J., Keenan F. P., 2009, MNRAS, 397, 903
- Krueger T. K. Czyzak S. J., 1970, Proc. R. Soc. Lond. A, 318, 531
- Leisy P., Dennefeld M., 2006, A&A, 456, 451
- Liu Y., Liu X.-W., Barlow M. J., Luo S.-G., 2004b, MNRAS, 353, 1251
- Liu Y., Liu X.-W., Luo S.-G., Barlow M. J., 2004a, MNRAS, 353, 1231
- Liu X.-W., Luo S.-G., Barlow M. J., Danziger I. J., Storey P. J., 2001, MNRAS, 327, 141
- Liu X.-W., Storey P. J., Barlow M. J., Danziger I. J., Cohen M., Bryce M., 2000, MNRAS, 312, 585
- Lodders K., 2010, in Principles and Perspectives in Cosmochemistry, eds. A. Goswami & B. E. Reddy, Astrophys. Space Sci. Proc. (Springer-Verlag), 379
- Luridiana V., Morisset C., Shaw R. A., 2014, preprint (arXiv:1410.6662)
- Marigo P., 2001, A&A, 370, 194
- McLaughlin B. M., Bell K. L., 2000, Journal of Physics B Atomic Molecular Physics, 33, 597
- Méndez R. H., 1989, IAUS, 131, 261
- Mendoza C., Zeppen C. J., 1982, MNRAS, 198, 127
- Milingo J. B., Kwitter K. B., Henry R. B. C., Souza S. P., 2010, ApJ, 711, 619
- Muñoz Burgos, J. M., Loch, S. D., Ballance, C. P., Boivin, R. F., 2009, A&A, 500, 1253
- Nataf D. M., Gould A. P., 2012, ApJ, 751, 39
- Nieva M.-F., Przybilla N., 2012, A&A, 539, 143
- Peimbert A., Peimbert M., 2010, ApJ, 724, 791
- Peimbert A., Peimbert M., Ruiz M. T., 2005, ApJ, 634, 1056
- Péquignot D., Walsh J. R., Zijlstra A. A., Dudziak G., 2000, A&A, 361, 1
- Pignatari M., et al., 2013, preprint (arXiv: 1307:6961)
- Podobedova L.I., Kelleher D.E., Wiese W.L., 2009, JPCRD, 38, 171
- Porter R. L., Ferland G. J., Storey P. J., Detisch M. J., 2012, MNRAS, 425, L28
- Porter R. L., Ferland G. J., Storey P. J., Detisch M. J., 2013, MNRAS, 433, L89
- Quiroza C., Rocha-Pinto H. J., Maciel W. J., 2007, A&A, 475, 217
- Ramsbottom C. A., Bell K. L., Keenan F. P., 1997, MNRAS, 284, 754
- Rodríguez M., Delgado-Inglada G., 2011, ApJ, 733, 50
- Rubin, R. H. 1986, ApJ, 309, 334
- Salpeter E. E., 1955, ApJ, 121, 161
- Sharpee B., Williams R., Baldwin J. A., van Hoof P. A. M., 2003, ApJS, 149, 157
- Simón-Díaz S., Stasińska G., 2008, MNRAS, 389, 1009
- Stasińska G., Peña M., Bresolin F., Tsamis Y. G., 2013, A&A, 552, 12
- Stasińska G., Tylenda R., Acker A., Stenholm B., 1991, A&A, 247, 173
- Stasińska G., et al., 2010, A&A, 511, AA44
- Storey P. J. 1994, A&A, 282, 999
- Storey P. J., Hummer D. G., 1995, MNRAS, 272, 41
- Storey P. J., Zeppen C. J., 2000, MNRAS, 312, 813
- Storey P. J., Sochi T., Badnell N. R., 2014, MNRAS, 441, 3028
- Tayal S. S., 2011, ApJS, 195, 12
- Tayal S.S., Gupta G.P., 1999 ApJ 526, 544
- Tayal S. S., Zatsarinny O., 2010, ApJS, 188, 32
- Tylenda R., Acker A., Stenholm B., 1993, A&AS, 102, 595
- Tsamis Y. G., Barlow M. J., Liu X.-W., Danziger I. J., Storey P. J., 2003, MNRAS, 345, 186
- Wang W., Liu X.-W., 2007, MNRAS, 381, 669
- Waters L. B. F. M., et al., 1998, A&A, 331, L61
- Wesson R., Liu X.-W., Barlow M. J., 2005, MNRAS, 362, 424
- Whittet D. C. B., 2003, Dust in Galactic Environment. IoP Publishing, Bristol
- Whittet D. C. B., 2010, ApJ, 710, 1009
- Zeppen C. J., 1982, MNRAS, 198, 111
- Zhang C. Y., 1995, ApJS, 98, 659